ACS Energy LETTERS

http://pubs.acs.org/journal/aelccp

Harnessing Cation Disorder for Enhancing Ionic Conductivity in Lithium Inverse Spinel Halides

Xiaochen Yang, Yu Chen,* Grace Wei, Mouhamad Said Diallo, Maxim Avdeev, Han-Ming Hau, Hao Qiu, Huiwen Ji, and Gerbrand Ceder*

Cite This: ACS Energy Lett. 2025, 10, 1338−1346

Read Online

ACCESS | Metrics & More | Article Recommendations | Supporting Information

ABSTRACT: Halides are promising solid-state electrolytes for all-solid-state lithium batteries due to their exceptional oxidation stability, high Li-ion conductivity, and mechanical deformability. However, their practicality is limited by the reliance on rare and expensive metals. This study investigates the Li_2MgCl_4 inverse spinel system as a cost-effective alternative. Molecular dynamics simulations reveal that lithium disordering at elevated temperatures significantly reduces the activation energy in Li_2MgCl_4. To stabilize this disorder at lower temperatures, we experimentally explored the $Li_xZr_{1-x/2}Mg_{x/2}Cl_4$ system and found that Zr doping induces both Zr and Li disorder at the 16c site at room temperature (RT). This leads to a 2 order-of-magnitude increase in ionic conductivity for the $Li_{1.25}Zr_{0.375}Mg_{0.625}Cl_4$ composition, achieving 1.4×10^{-5} S cm^{-1} at RT, compared to pristine Li_2MgCl_4. By deconvoluting the role of lithium vacancies and dopants, we reveal that cation disordering to the 16c site predominantly enhances ionic conductivity, whereas lithium vacancy concentration has a very limited effect.

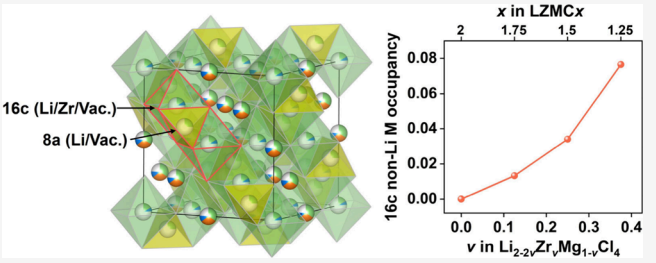

Solid-state batteries (SSBs) have gained tremendous interest due to their superior safety and energy density compared to traditional Li-ion batteries.[1−4] Unlike liquid electrolytes, which are prone to leakage, flammability, and chemical degradation over time,[5] solid-state electrolytes (SSEs) offer enhanced thermal stability, reducing the risks associated with battery failure. Additionally, SSEs may provide a wider electrochemical stability window,[6] potentially enabling the use of high-voltage cathodes and Li metal anode for enhanced energy density.

Among the various classes of SSEs, halides have recently emerged as particularly promising candidates.[7−10] Following the discovery of the Li_3YCl_6 superionic conductor,[11] which achieves a room temperature (RT) ionic conductivity of 0.5 mS cm^{-1} via mechanochemical synthesis, ternary halides with the general formula Li_aMX_b (where M represents a metal cation and X represents a halide anion) have been extensively investigated.[10,12,13] Chloride-based SSEs are of special interest due to their high Li-ion conductivity, good deformability, and excellent stability and compatibility with high-voltage cathodes.[14,15] Despite these advantages, many reported halide SSEs rely on rare and expensive metals such as Y, Sc, and In.[16−18] While these metals are essential for achieving high ionic conductivity, they significantly increase material costs, making them economically challenging for large-scale applications. Additionally, most halide SSEs are unstable with lithium metal anodes, where reduction-driven decomposition forms a rapidly growing interphase that degrades cell performance.[19]

To address these challenges, there is a strong motivation to explore cost-effective chloride-based Li-ion conductors. The Li_2MgCl_4 inverse spinel system is promising due to the abundance and low cost of magnesium. Initially investigated in the 1970s, Li_2MgCl_4 with an inverse spinel structure exhibits ionic conductivities of approximately 10^{-3} to 10^{-1} S cm^{-1} at elevated temperatures (200−400 °C).[20−22] However, its RT ionic conductivity is limited to approximately 10^{-7} S cm^{-1}.[21] A distinct knee in the Arrhenius plot of ionic conductivities is observed around 300 °C, featuring a significant decrease of the activation energy beyond this transition temperature.[20] This behavior implies that the RT ionic conductivity of Li_2MgCl_4

Received: January 8, 2025
Revised: February 9, 2025
Accepted: February 11, 2025

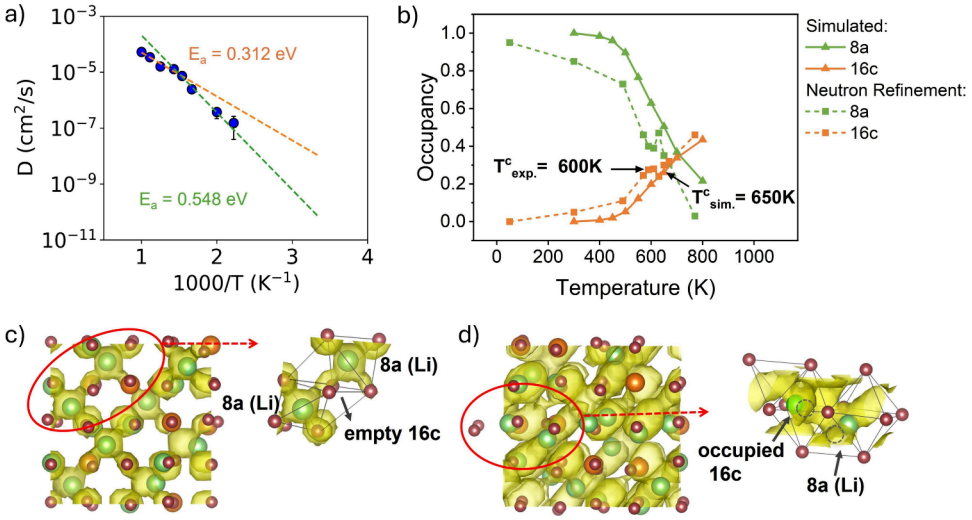

Figure 1. (a) Arrhenius plot of MD-simulated Li-ion diffusivities in Li_2MgCl_4 across a temperature range of 450 to 1000 K. (b) Temperature-dependent occupancies of Li in the 8a and 16c sites in Li_2MgCl_4 structure. Solid lines represent MD simulation results, while dashed lines indicate neutron diffraction refinement data (adapted from[28]). Calculated Li-ion probability densities and structures in Li_2MgCl_4 at (c) 500 K and (d) 700 K, based on MD simulations. Li, Mg, and Cl atoms are shown in green, orange, and dark pink, respectively. In the enlarged plot of (d), the gray dashed circles represent the undistorted 8a and 16c sites.

may be greatly enhanced if the high-temperature phase can be stabilized at RT. Furthermore, studies on off-stoichiometric $Li_{2-2x}Mg_{1+x}Cl_4$ have shown that substituting Mg^{2+} for Li^+ increases RT Li-ion conductivity to ~10^{-6} S cm^{-1} by creating extra cation vacancies.[21]

Recent studies have revisited the Li_2MgCl_4 inverse spinel system, exploring the effects of off-stoichiometry and aliovalent ion doping on improving its RT ionic conductivity.[23−25] For example, divalent Zn^{2+} doping in $Li_{1.6}Zn_{0.2}MgCl_4$ results in an RT ionic conductivity of 1.2 × 10^{-5} S cm^{-1}.[23] Trivalent Al^{3+} doping in the Li-deficient composition $Li_{1.2}Mg_{1.4}Cl_4$ to $Li_{1.2}Mg_{0.95}Al_{0.3}Cl_4$ increases RT ionic conductivity by 2 orders of magnitude to 3 × 10^{-4} S cm^{-1}.[24] Additionally, tetravalent Zr^{4+} doping in $Li_2Mg_{1/3}Zr_{1/3}Cl_4$ achieves an RT conductivity of 2.8 × 10^{-5} S cm^{-1}.[25] These ionic conductivity enhancements have been primarily attributed to the creation of extra Li vacancies through doping. However, among these reports, compositions with identical lithium content can exhibit widely different ionic conductivities depending on the dopant introduced,[23−25] indicating that factors beyond lithium vacancy concentration influence ionic conductivity. Therefore, it is crucial to deconvolute the specific roles of dopants and lithium vacancies and deepen our understanding of the underlying Li-ion conduction mechanisms to fully unlock the potential of this system.

In this work, we systematically investigated the Li−Mg−Cl inverse spinel system, focusing on the correlation between crystal structure and ionic conductivity induced by aliovalent ion doping. Molecular dynamics simulations reveal that lithium occupation of the 16c site at elevated temperature significantly reduces the activation energy for Li-ion conduction in pristine Li_2MgCl_4. Experimentally, we synthesized and characterized $Li_xZr_{1-x/2}Mg_{x/2}Cl_4$ samples (LZMC*x*, where *x* represents the lithium concentration) and found that both Zr and Li partially occupy the 16c site, which is vacant in pristine Li_2MgCl_4. This cation disordering leads to a two-order-of-magnitude increase in the ionic conductivity for the LZMC1.25 sample compared to pristine Li_2MgCl_4, reaching 1.4 × 10^{-5} S cm^{-1} at RT. Furthermore, by studying a series of samples with various levels of lithium vacancies and doping concentrations, as well as controlling the dopant type and the level of dopant disordering, we unveil that cation disordering at the 16c site plays a crucial role in enhancing Li-ion conduction, while the impact of lithium vacancy concentration on ionic conductivity is found to be relatively limited in this system.

MACHINE LEARNING-BASED MOLECULAR DYNAMICS SIMULATION OF LI_2MGCL_4

To investigate Li-ion transport in inverse spinel systems, we employed a machine learning interatomic potential (MLIP) to perform molecular dynamics (MD) simulations on Li_2MgCl_4. Our MLIP was fine-tuned from the pretrained CHGNet[26] model using DFT-calculated energies, interatomic forces, and stresses from various atomic configurations of Li_2MgCl_4 sampled via FLARE.[27] Each MLIP-MD simulation was performed for 2 ns.

Figure 1a presents the simulated Li-ion diffusivities of Li_2MgCl_4 across a temperature range of 450 to 1000 K. The diffusivities exhibit a change of slope in the Arrhenius plot at $T_{sim.}^{c}$ = 650 K. Below 650 K, the calculated activation energy $E_a^{L.T.}$ is 0.548 eV, while above 650 K, a significantly lower activation energy of $E_a^{H.T.}$ = 0.312 eV is observed. Our MD simulations are consistent with the experimentally observed non-Arrhenius behavior reported by Cros et al.,[20] which shows a transition temperature $T_{exp.}^{c}$ = 600 K, with activation energies of $E_a^{L.T.}$ = 0.57 eV and $E_a^{H.T.}$ = 0.34 eV.

To understand the reason for the abrupt change in the activation energy, we examined the lithium occupancies in the MD configurations derived from pristine Li_2MgCl_4 as a function of temperature from 300 to 800 K. As shown by the solid line in Figure 1b, the 8a Li occupancy gradually decreases with increasing temperature, accompanied by a corresponding increase in the 16c Li occupancy. The occupancy of Mg and Li in 16d sites remains largely unchanged, with minimal 16d to 8b site disordering above 650 K (8b site occupancy remains below 0.05, Figure S1). These results suggest that Li ions gradually disorder from 8a to 16c sites as the temperature increases. The simulated Li

https://doi.org/10.1021/acsenergylett.5c00078
ACS Energy Lett. 2025, 10, 1338−1346

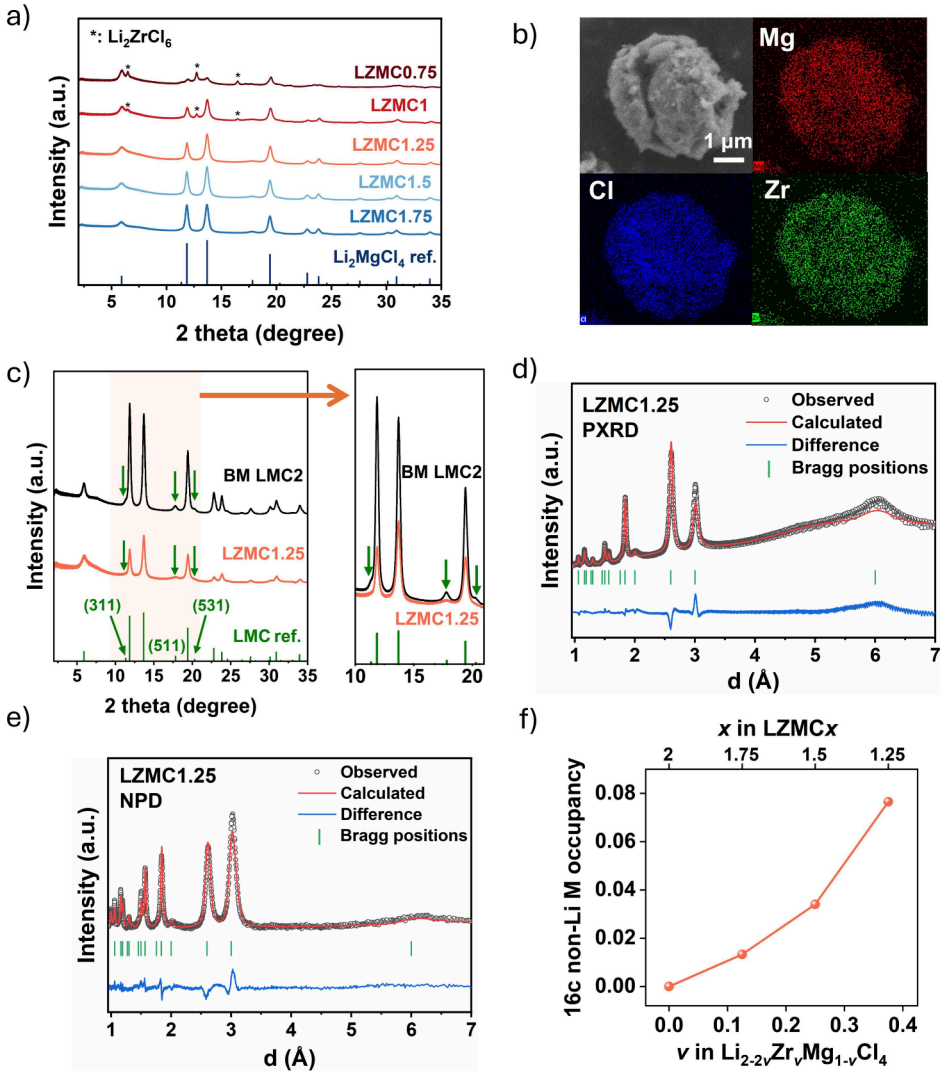

Figure 2. (a) Synchrotron XRD patterns of the LZMC*x* series. Bragg positions of the Li_2MgCl_4 phase are labeled by vertical tick marks, and impurity peaks from Li_2ZrCl_6 are marked with asterisks. (b) SEM image of a LZMC1.25 particle with corresponding EDS mapping of Mg, Cl, and Zr. (c) Synchrotron XRD patterns of ball-milled LMC2 and LZMC1.25. Dark green arrows indicate the positions of the 311, 511, and 531 peaks. (d) synchrotron XRD and (e) Neutron powder diffraction patterns of LZMC1.25 with Rietveld refinements. (f) The 16c non-Li metal occupancy as a function of Zr concentration (v) in $Li_{2-2v}Zr_vMg_{1-v}Cl_4$.

occupancies align well with the refined occupancies from a previous neutron diffraction study on Li_2MgCl_4,[28] shown as dashed lines in Figure 1b. Notably, both simulated and experimentally observed transition temperatures $T_{sim.}{}^c$ and $T_{exp.}{}^c$ occur when the lithium 16c occupancy reaches approximately 0.25.

We further visualized the simulated structures and Li-ion probability densities averaged over MD trajectories at 500 and 700 K, as shown in Figure 1c and 1d, respectively. At both temperatures, Li ions are observed to hop between tetrahedral 8a sites via intermediate 16c octahedral sites, while Li ions in 16d sites remain immobile. Below the transition temperature at 500 K, Li ions fully occupy the 8a sites, with all 16c sites remaining vacant (Figure 1c). At 700 K, however, partial disordering of Li from 8a to 16c sites is observed, with face-sharing 8a and 16c Li exhibiting out-of-center distortion (Figure 1d). This face-sharing Li configuration can greatly flatten the energy landscape for Li-ion migration and lower the activation energy, as recently reported in the overstoichiometric fcc-type Li−In−Sn-O compound[29] and in overlithiated lithium titanate spinels.[30] Below the transition temperature, no Li disordering is observed and Li_2MgCl_4 exhibits a low ionic conductivity of approximately 10^{-7} S cm^{-1} at room temperature. Nevertheless, if one extrapolates ionic conductivity based on the low activation energy observed at high temperatures (above 600 K), an RT ionic conductivity of around 10^{-3} S cm^{-1} would be achieved. This suggests that stabilizing Li disordering to the 16c site at RT can potentially create high ionic conductivity in the Li−Mg−Cl inverse spinel system.

STRUCTURAL CHARACTERIZATION OF $Li_xZr_{1-x/2}Mg_{x/2}Cl_4$ SYSTEMS

Ion doping is a common strategy to induce lithium disorder. To stabilize the Li disorder at the 16c sites in the inverse spinel system, we investigated a series of Zr-doped Li_2MgCl_4 compounds. Zr was selected as the dopant due to its cost-effectiveness and greater abundance compared to rare earth or post-transition metals like Y or In.[13] Specifically, we prepared samples of $Li_xZr_{1-x/2}Mg_{x/2}Cl_4$ (denoted as LZMC*x*, where *x*

https://doi.org/10.1021/acsenergylett.5c00078
ACS Energy Lett. 2025, 10, 1338−1346

Table 1. Crystallographic Data of LZMC1.25[a] as Obtained from Rietveld Corefinement of X-ray and Neutron Powder Diffraction Data[b]

Atom	Site	x	y	z	U_{iso} (Å^2)	Occupancy
Li1	8a	0.125	0.125	0.125	0.037(4)	0.220(22)
Li2	16d	0.5	0.5	0.5	0.037(4)	0.337(19)
Li3	16c	0	0	0	0.037(4)	0.178(22)
Mg1	16d	0.5	0.5	0.5	0.0176(8)	0.307(5)
Mg2	16c	0	0	0	0.0176(8)	0.005(5)
Zr1	16d	0.5	0.5	0.5	0.0176(8)	0.116(2)
Zr2	16c	0	0	0	0.0176(8)	0.071(2)
Cl1	32e	0.25625(7)	0.25625(7)	0.25625(7)	0.0182(2)	1

[a]$Li_{1.25}Zr_{0.375}Mg_{0.625}Cl_4$: a = 10.3907(5) Å ($Fd\bar{3}m$). [b]R_w = 3.68%, GOF = 1.48.

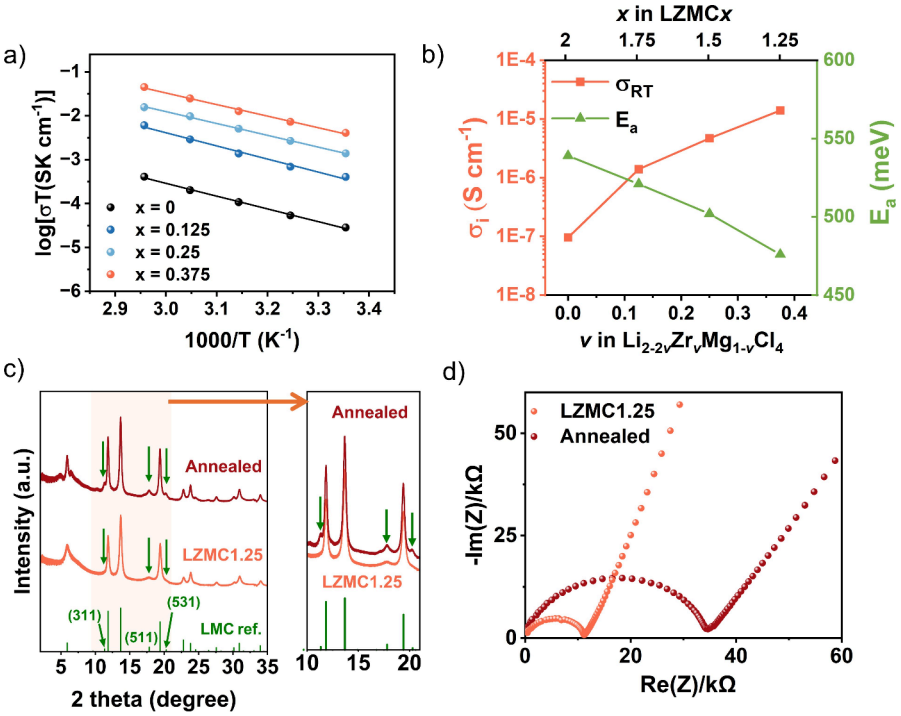

Figure 3. (a) Arrhenius plots of ionic conductivity for LMC2 and LZMCx samples from variable-temperature EIS measurements. (b) Comparison of RT ionic conductivities and activation energies for LZMCx samples. (c) Synchrotron XRD patterns of as-prepared and annealed LZMC1.25. Dark green arrows indicate the positions of the 311, 511, and 531 peaks. (d) Nyquist plots of as-prepared and annealed LZMC1.25 from EIS measurement at RT.

represents the lithium concentration) via high-energy ball milling of LiCl, $MgCl_2$, and $ZrCl_4$ precursors. For comparison, Li_2MgCl_4 (LMC2) was also synthesized using the same mechanochemical approach. Figure 2a presents synchrotron X-ray diffraction (XRD) patterns of the LZMCx samples. The diffraction peaks of LZMC1.75, LZMC1.5, and LZMC1.25 align well with the Li_2MgCl_4 inverse spinel phase, confirming successful Zr incorporation. However, further increasing the Zr dopant concentration to LZMC1 and LZMC0.75 results in the formation of a Li_2ZrCl_6 impurity phase, whose diffraction peaks are marked by the asterisks in Figure 2a. This suggests that the solubility limit of Zr in the Li_2MgCl_4 structure is approximately reached for x = 1.25. Crystallinity analysis via Rietveld refinement with Ag as an internal standard confirms that the LZMC1.25 sample is mostly crystalline, with less than 5 wt % amorphous content (see Supplementary Note 1). The scanning electron microscopy (SEM) image of the LZMC1.25 sample (Figure 2b) shows an average particle size of approximately 5 μm. Energy dispersive X-ray spectroscopy (EDS) mapping shows a uniform elemental distribution, further confirming the single-phase nature of the Zr-doped sample.

The synchrotron XRD patterns of ball-milled LMC2 and LZMC1.25 are compared in Figure 2c. While both samples exhibit the inverse spinel phase, LZMC1.25 shows a significant reduction in intensity for the 311, 511, and 531 peaks. To rationalize this, we simulated the XRD peak intensity for these planes based on their structure factors and determined the metal occupancies that can match the observed intensity reduction (details provided in Supplementary Note 1). This analysis reveals that the intensity for the 311, 511, and 531 planes is reduced when nonlithium metals (Zr/Mg) partially occupy the 16c site, with the site occupancies described by the equation Zr_16c_occ. + 0.284 × Mg_16c_occ. = 0.0726 providing the best fit (Supplementary Note 2, Figure S15). Based on the above analysis, Rietveld corefinement of neutron powder diffraction (NPD) and synchrotron XRD data were further performed to resolve the fine structure of LZMC1.25,

https://doi.org/10.1021/acsenergylett.5c00078
ACS Energy Lett. 2025, 10, 1338−1346

as shown in Figure 2d and 2e. The resulting structural parameters are provided in Table 1. In LZMC1.25, Zr atoms are found to be distributed in both the 16d and 16c sites, with occupancies of 0.116 and 0.071, respectively, while nearly all Mg atoms occupy the 16d site. Li atoms are refined to the 8a, 16d, and 16c sites, with occupancies of 0.220, 0.337, and 0.178 respectively.

The disordering of lithium into the 16c site likely stems from the presence of Zr in the 16c site. Since the 16c site face shares with the 8a site, partial Zr occupancy at the 16c site will raise the energy of the adjacent 8a site, driving the 8a Li to migrate into an empty 16c site, thereby facilitating 8a-16c Li disorder at a much lower temperature than in pristine Li_2MgCl_4. A similar effect has been observed in the spinel oxide $LiNi_{0.5}Mn_{1.5}O_4$, where Ni disorder from the 16d to the 16c site promotes lithium disorder from the 8a to the 16c site. Rietveld corefinements for LZMC1.75, LZMC1.5, and LMC2 samples were also performed (Figure S2−4), with structural parameters detailed in Tables S1 and S2. Figure 2f illustrates the relationship between 16c nonlithium metal occupancy and Zr concentration (v) in $Li_{2-2v}Zr_vMg_{1-v}Cl_4$, demonstrating that higher Zr doping levels lead to an increased Zr occupancy at the 16c site.

LI-ION CONDUCTIVITIES OF LZMC

The Li-ion conductivities of the LZMC and LMC2 samples were measured using electrochemical impedance spectroscopy (EIS). Approximately 50 mg of the sample powder was uniaxially pressed into pellets under 300 MPa, with stainless steel rods as ion-blocking electrodes. Ionic conductivity values were determined through equivalent circuit fitting of the EIS spectra (see Supplementary Note 3, Figures S16 and S17, and Table S7). Figure S5 presents the Nyquist plots at RT (25 °C), and Figure 3a shows Arrhenius plots of the ionic conductivities from variable-temperature EIS measurements (15−55 °C) for LZMC and LMC2 samples. The RT ionic conductivities and activation energies, derived from the Nyquist and Arrhenius plots, are summarized in Figure 3b. The results show that increasing Zr dopant concentration enhances ionic conductivity and reduces the activation energy. LZMC1.25 exhibited the highest RT ionic conductivity of 1.4×10^{-5} S cm^{-1}, 2 orders of magnitude greater than that of LMC2 (9.6×10^{-8} S cm^{-1}). It also demonstrates the lowest activation energy of 476 meV, lower than that of pristine LMC2 (539 meV). Error analysis, performed on LZMC1.25 as a representative example, shows a relative standard deviation of 2.32%, indicating high reproducibility across measurements (see Supplementary Note 4). A d.c. polarization test indicates an electronic conductivity of 2.2×10^{-9} S cm^{-1} at RT for LZMC1.25 (Figure S6), which is 4 orders of magnitude lower than its ionic conductivity, confirming the predominantly ionic-conducting nature of the material.

From the above synchrotron XRD and NPD corefinement results, we found that Li and Zr ions are partially disordered to the 16c site upon Zr doping, with 16c site occupancy increasing as the Zr content rises. We thus hypothesize that the enhanced ionic conductivity upon Zr doping may be attributed to this cation disordering, which has been computationally shown in other close-packed halides to improve lithium conductivity. To verify this hypothesis, we annealed the LZMC1.25 sample at 200 °C for 24 h, as cation disorder is expected to be metastable and may diminish upon annealing. Figure 3c presents the synchrotron XRD patterns of the annealed LZMC1.25 sample, which show diffraction peaks corresponding to the inverse spinel phase, along with a few low-intensity reflections (e.g., near 6°, 10°, and 16°). Identifying this impurity phase is challenging due to the limited number of peaks observed, which are confined to the low two-theta region. However, impurity is likely present only in small amounts, as suggested by its low intensity in the XRD pattern. For the primary inverse spinel phase, the annealed sample exhibits significantly increased intensities of the 311, 511, and 531 peaks compared to the as-prepared LZMC1.25, closely resembling those of pristine LMC2 (Figure 2c). This suggests a decrease in Zr occupancy at the 16c site in the annealed sample, i.e., most Zr ions occupy the 16d site and the level of Zr disorder is reduced. Rietveld refinement further confirms that Zr occupancy at the 16c site decreases from 0.071 in the as-prepared LZMC1.25 to 0.017 in the annealed sample (Table S3). To address concerns regarding the possible volatilization of $ZrCl_4$ during annealing, we performed thermogravimetric analysis (TGA) on pristine and annealed LZMC1.25 samples, as shown in Figure S7. The TGA results reveal negligible weight loss in pristine LZMC1.25 up to 225 °C, confirming minimal $ZrCl_4$ volatilization.

Figure 3d shows the Nyquist plots of the as-prepared and annealed LZMC1.25 from EIS measurement at RT. The measured ionic conductivity of LZMC1.25 decreases from 1.4×10^{-5} S cm^{-1} to 5.4×10^{-6} S cm^{-1} after annealing (equivalent circuit fitting shown in Figure S18 and Table S8). This drop in ionic conductivity of annealed LZMC1.25 proves that Zr disordering to the 16c site can indeed facilitate faster Li-ion conduction, likely by promoting Li disordering from the 8a to the16c site, which is expected to decrease the energy difference between these sites for Li to hop through.

Electrochemical stability and interfacial compatibility of LZMC1.25 with lithium metal were evaluated through linear sweep voltammetry (LSV), time-resolved EIS, and galvanostatic cycling, as detailed in Supplementary Note 5. These studies reveal that LZMC1.25 exhibits an electrochemical stability window of 1.03−3.81 V and demonstrates superior reduction stability compared to Li_2ZrCl_6. However, the interphase at the Li-electrolyte interface remains nonpassivating, suggesting that LZMC1.25 may be better suited as a catholyte.

IMPACT OF DOPANT DISORDER ON LI-ION CONDUCTIVITY

Building on our observation that Zr disorder benefits Li-ion conductivity, we expanded our search by exploring the effects of different aliovalent dopants. Specifically, we synthesized two additional doped samples: $Li_{1.25}Ta_{0.25}Mg_{0.75}Cl_4$ (LTMC1.25) and $Li_{1.25}In_{0.375}Mg_{0.8125}Cl_4$ (LIMC1.25), with a fixed Li content of 1.25 to ensure a consistent Li vacancy level across all samples. XRD patterns in Figure 4a confirm that both samples exhibit a single-phase inverse spinel. However, unlike LZMC1.25, neither LTMC1.25 nor LIMC1.25 shows a reduction in the intensity of the 311, 511, and 531 peaks as compared with pure LMC2. To further clarify the structure of LTMC1.25 and LIMC1.25, we performed synchrotron XRD Rietveld refinements, as shown in Figure S8. The resulting crystallographic data is summarized in Table S4. The refinements reveal that both Ta^{5+} and In^{3+} reside exclusively on the 16d site, with no significant disorder in the 16c site. Attempts to assign Ta^{5+} or In^{3+} to the 16c site during refinement resulted in a notable mismatch between calculated

https://doi.org/10.1021/acsenergylett.5c00078
ACS Energy Lett. 2025, 10, 1338−1346

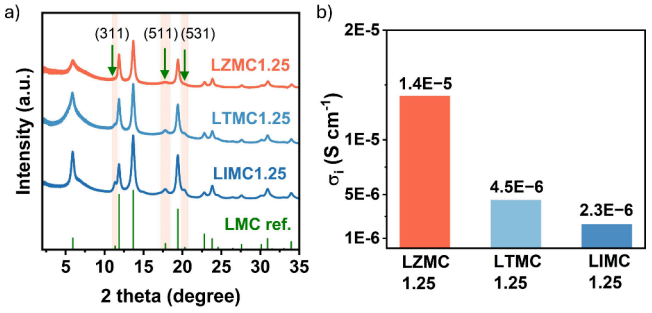

Figure 4. (a) Synchrotron XRD patterns of LZMC1.25, LTMC1.25, and LIMC1.25. The Bragg positions of the Li_2MgCl_4 phase are labeled by vertical tick marks. The dark green arrows highlight the positions of the 311, 511, and 531 peaks. (b) Ionic conductivities of LZMC1.25, LTMC1.25, and LIMC1.25 from EIS measurement at RT.

and observed peak intensities, particularly for the 311 and 531 peaks. This suggests that neither Ta nor In is likely to induce significant cation disordering to the 16c site, in contrast to Zr doping.

The RT ionic conductivities of LTMC1.25 and LIMC1.25, determined via EIS (Nyquist plots and equivalent circuit fitting in Figure S19 and Table S9), are compared with LZMC1.25 in Figure 4b. LTMC1.25 and LIMC1.25 exhibit RT ionic conductivities of 4.5×10^{-6} and 2.3×10^{-6} S cm^{-1}, respectively, both much lower than that of LZMC1.25 (1.4×10^{-5} S cm^{-1}). These results further emphasize the important role of cation disordering to the 16c site in enhancing ionic conductivity. Despite being effective dopants in other solid electrolyte systems, Ta^{5+} and In^{3+} doping in the Li_2MgCl_4 inverse spinel lattice fail to induce similar cation disordering as Zr^{4+}, resulting in low RT ionic conductivities. This highlights the importance of dopant chemistry and its impact on structural regulation, extending beyond the mere creation of Li vacancies.

DECONVOLUTING THE IMPACT OF LITHIUM VACANCIES AND DOPANT DISORDER

The increase in lithium vacancy concentration has been prevalently regarded as the primary factor that accounts for the enhanced ionic conductivity in the reported doped LMC system.[23−25] To evaluate if the creation of lithium vacancies is a dominant factor, we study a series of $Li_xMg_{2-x/2}Cl_4$ (LMCx, x = 1.25, 1.5, 1.75, 2) samples, where lithium vacancies were introduced via Mg off-stoichiometry instead of aliovalent ion doping. Figure S10a displays the XRD patterns for the LMCx samples that were synthesized by the same mechanochemical method, all of which exhibit a single-phase inverse spinel. Arrhenius plots of temperature-dependent ionic conductivities for the LMCx compounds are presented in Figure S10b,c, which summarizes their ionic conductivities and activation energies.

Among the four LMCx samples, LMC1.5 exhibited the highest RT ionic conductivity of 8×10^{-7} S cm^{-1} with an activation energy of 531 meV. Notably, despite having a higher concentration of lithium vacancies, LMC1.25 exhibits a lower conductivity of 6.10×10^{-7} S cm^{-1}, which is 20 times lower than that of LZMC1.25. Additionally, the activation energies show minimal variation across the LMCx samples, with the lowest barrier observed in LMC1.75 at 525 meV (compared to 539 meV for pristine LMC2). These results suggest that lithium vacancies have a limited effect on the ionic conductivity and activation energy in this inverse spinel system. Therefore, the significantly higher conductivity observed in LZMC1.25 must be attributed to the Zr disorder.

To further deconvolute the effects of lithium vacancies and dopant disordering on ionic conductivity, we synthesized five new compositions with the general formula $Li_uZr_vMg_wCl_4$ using the same ball-milling method. The new compositions include $Li_{2.2}Zr_{0.2}Mg_{0.5}Cl_4$, $Li_2Zr_{0.2}Mg_{0.6}Cl_4$, $Li_2Zr_{0.3}Mg_{0.4}Cl_4$, $Li_{1.8}Zr_{0.3}Mg_{0.5}Cl_4$, and $Li_{1.6}Zr_{0.4}Mg_{0.4}Cl_4$. Synchrotron XRD patterns (Figure S11) confirm that all five compositions crystallize as single-phase inverse spinel. Their Nyquist plots with corresponding fit to the equivalent circuit are detailed in Figure S20 and Table S10, and Arrhenius plots derived from temperature-dependent EIS measurements are depicted in Figure S12. In this new series, both the dopant and Mg concentrations are varied to achieve different levels of lithium deficiency/vacancies. Given that lithium can occupy both 8a and 16d sites, with the 16d sites also shared by Mg and Zr, a deficiency of non-Li metal cations in the 16d site can result in a redistribution of Li occupancies between 8a and 16d sites, which is effectively equivalent to the creation of Li vacancies in 8a/16d sites. Thus, the cation deficiency level for a composition of $Li_uZr_vMg_wCl_4$ is defined as 3-u-v-w, which directly reflects the cation vacancy content compared to the stoichiometric spinel with cation/anion ratio of 3/4. Figure 5a

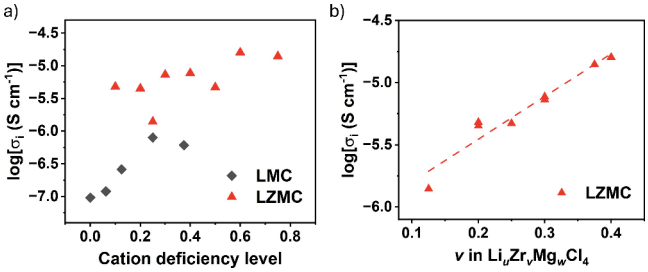

Figure 5. Room temperature ionic conductivity as a function of (a) cation deficiency level in LMC and LZMC samples, and (b) Zr concentration (v) in $Li_uZr_vMg_wCl_4$.

plots the cation deficiency level versus RT ionic conductivity for LZMC and LMC samples. (Detailed ionic conductivities and activation energies are summarized in Table S5). The LZMC group plotted in Figure 5a includes both previous $Li_xZr_{1-x/2}Mg_{x/2}Cl_4$ (x = 1.25, 1.5, and 1.75) samples and the five new compositions.

For the $Li_xMg_{2-x/2}Cl_4$ (LMC) system, a positive correlation between ionic conductivity and cation deficiency is observed, consistent with previous reports.[21] However, across different chemical spaces, doped samples exhibit significantly higher ionic conductivity at the same cation deficiency level than LMC. Among these, the LZMC samples (red points) demonstrate the highest ionic conductivity across all levels of cation deficiency. Notably, within the LZMC samples, there is no apparent correlation between cation deficiency and ionic conductivity. Instead, Figure 5b shows a strong correlation between ionic conductivity and Zr concentration (v in $Li_uZr_vMg_wCl_4$), with samples with the same Zr concentration exhibiting similar ionic conductivities, regardless of cation deficiency level. Given that the Zr occupancy in the 16c site is proportional to the Zr concentration (Figure 2f), we conclude that cation disordering to the 16c site plays a dominant role in

https://doi.org/10.1021/acsenergylett.5c00078
ACS Energy Lett. 2025, 10, 1338−1346

enabling facile Li-ion conduction in LZMC samples, whereas the cation vacancy content has a very limited impact.

Understanding ion diffusion mechanisms and their correlation with structural features is essential for the rational design of SSEs. Our MD simulations of pristine Li_2MgCl_4 reveal that Li-ion diffusion occurs via 8a to 16c site hopping, consistent with the observations in other oxide spinels.[31] The activation energy drop near 650 K, coinciding with lithium disordering from 8a to 16c sites, suggests that stabilizing this disorder at RT can enhance ionic conductivity. Our systematic investigation of Zr-doped LZMC*x* compounds indicates that Zr doping leads to partial occupation of the 16c site by both Zr and Li, contributing to the increased RT ionic conductivity. The optimized LZMC1.25 composition achieves an RT ionic conductivity of 1.4×10^{-5} S cm^{-1}, a two-order-of-magnitude improvement over pristine Li_2MgCl_4. Zr occupancy at the 16c site has been observed and reported in a previous study,[25] where it was considered detrimental to Li-ion diffusion due to its potential to block diffusion channels. However, given the relatively low occupancy of Zr at the 16c site (around 0.07), we believe there is no apparent blocking effect. Instead, we hypothesize that the presence of Zr at the 16c site likely raises the site energy of the face-sharing 8a site for Li and induces the desired lithium disordering to the 16c site, facilitating facile ion conduction along an 8a-16c-8a pathway with a lower activation energy. The ionic conductivity drops caused by the removal of cations from the 16c site, either through annealing or substitution with other dopants, further confirms that cation disordering to the 16c site is critical for Li-ion conduction in this system.

Previous studies[23−25] have attributed ionic conductivity enhancement in doped Li_2MgCl_4 primarily to increases in the lithium vacancy concentration, often without deconvoluting the roles of vacancies and dopants. Our comparative study with lithium-deficient, undoped LMC samples reveals that, despite similar cation deficiency levels, LZMC consistently exhibits superior ionic conductivities and lower activation energies. This indicates that Zr doping and the resulting cation disorder, rather than vacancies, are key to enhanced Li-ion transport. There is indeed synergy between 16*d*/16c cation ordering and the strong preference of Li for the 8a site. The empty 16c site in ordered spinel creates the ideal electrostatic environment for Li in 8a, and perturbation of the 16*c*/16d is therefore likely to increase the 8a energy, making Li more mobile. While the beneficial effect of 16c occupancy in a spinel has been observed in ball-milled oxides,[32] it is rarely found as an equilibrium disorder.

Nevertheless, the activation energy in LZMC1.25 (476 meV) remains higher than in pristine Li_2MgCl_4 above the transition temperature (312 meV). This discrepancy likely stems from the absence of face-sharing Li configurations in LZMC due to the reduced lithium content caused by the tetravalent Zr^{4+} doping. In pristine Li_2MgCl_4, with 2 Li/formula unit (f.u.), Li fully occupies the 8a site and any Li disordering to the 16c site will lead to 8a-16c face-sharing Li configurations. In contrast, in LZMC, Zr^{4+} doping decreases the Li content to less than 2 Li/f.u., creating vacancies at the 8a site. This enables Li ions to disorder from the 8a site to the 16c site without creating 8a-16c face-sharing. The fact that LZMC can avoid the high-energy face-sharing configurations makes lithium disordering to the 16c site more accessible than in pristine Li_2MgCl_4. Additionally, Zr disordering at the 16c site in LZMC further promotes Li disorder, stabilizing 16c Li at RT. Face-sharing Li configurations are known to significantly lower the activation energy and promote fast ion conduction, as reported in the disordered $Li_2Sc_{2/3}Cl_4$ spinel-type superionic conductor (1.5 mS cm^{-1}, 0.34 eV),[17] the overstoichiometric rocksalt Li−In−Sn-O compound (0.34 mS cm^{-1}, 0.255 eV),[29] and in overlithiated spinel oxides.[33] Hence, the absence of face-sharing Li configuration in LZMC limits its activation energy for Li-ion conduction from reaching values as low as that of pristine Li_2MgCl_4 above the transition temperature. The trend in activation energies can be explained as follows: E_a (Li in 8a and 16c sites, face-sharing) < E_a (Li in 8a and 16c sites, nonface-sharing) < E_a (Li only in 8a). Increasing lithium concentration by employing high-valent anion substitution (e.g., oxygen or nitrogen) could potentially enable face-sharing configurations, further reducing activation energy and improving conductivity.

In this study, we demonstrate that cation disordering to the 16c site, induced by Zr doping in the Li_2MgCl_4 inverse spinel system, enhances the ionic conductivity, resulting in a two-order-of-magnitude improvement to 1.4×10^{-5} S cm^{-1} at room temperature for the $Li_{1.25}Zr_{0.375}Mg_{0.625}Cl_4$ composition. We further challenge the conventional emphasis on creating lithium vacancies to enhance ionic conductivity, revealing that lithium vacancies alone have a very limited impact on this system. These findings provide new insights into designing cost-effective inverse spinel-based solid electrolytes with low activation energies.

■ ASSOCIATED CONTENT

Supporting Information

The Supporting Information is available free of charge at https://pubs.acs.org/doi/10.1021/acsenergylett.5c00078.

Detailed description of the mechanochemical synthesis and characterization of inverse spinel halides, structural corefinement based on synchrotron XRD and neutron powder diffraction, crystallinity assessment via Rietveld refinement, simulated XRD intensity analysis for site occupancy determination, electrochemical analysis including EIS fitting, LSV, d.c. polarization, and galvanostatic cycling tests, computational details of evaluating Li-ion transport properties using DFT and machine-learning interatomic potentials for MD simulations, and halide inverse spinel conductor (PDF)

■ AUTHOR INFORMATION

Corresponding Authors

Yu Chen − *Department of Materials Science and Engineering, University of California, Berkeley, California 94720, United States; Materials Sciences Division, Lawrence Berkeley National Laboratory, Berkeley, California 94720, United States;* orcid.org/0000-0002-5420-7571; Email: yu_chen@berkeley.edu

Gerbrand Ceder − *Department of Materials Science and Engineering, University of California, Berkeley, California 94720, United States; Materials Sciences Division, Lawrence Berkeley National Laboratory, Berkeley, California 94720, United States;* orcid.org/0000-0001-9275-3605; Email: gceder@berkeley.edu

Authors

Xiaochen Yang − *Department of Materials Science and Engineering, University of California, Berkeley, California*

94720, United States; Materials Sciences Division, Lawrence Berkeley National Laboratory, Berkeley, California 94720, United States

Grace Wei − *Department of Materials Science and Engineering, University of California, Berkeley, California 94720, United States; Materials Sciences Division, Lawrence Berkeley National Laboratory, Berkeley, California 94720, United States;* orcid.org/0000-0002-4211-1927

Mouhamad Said Diallo − *Department of Materials Science and Engineering, University of California, Berkeley, California 94720, United States; Materials Sciences Division, Lawrence Berkeley National Laboratory, Berkeley, California 94720, United States*

Maxim Avdeev − *Australian Nuclear Science and Technology Organisation, Kirrawee DC, New South Wales 2232, Australia; School of chemistry, University of Sydney, Sydney, New South Wales 2006, Australia;* orcid.org/0000-0003-2366-5809

Han-Ming Hau − *Department of Materials Science and Engineering, University of California, Berkeley, California 94720, United States; Materials Sciences Division, Lawrence Berkeley National Laboratory, Berkeley, California 94720, United States*

Hao Qiu − *Department of Materials Science and Engineering, University of California, Berkeley, California 94720, United States*

Huiwen Ji − *Department of Materials Science and Engineering, University of Utah, Salt Lake City, Utah 84112, United States;* orcid.org/0000-0001-8091-9428

Complete contact information is available at: https://pubs.acs.org/10.1021/acsenergylett.5c00078

Author Contributions

X.Y. and Y.C. contributed equally to this paper.

Notes

The authors declare no competing financial interest.

■ ACKNOWLEDGMENTS

This research used 7BM of the National Synchrotron Light Source II, a U.S. Department of Energy (DOE) Office of Science User Facility operated for the DOE Office of Science by Brookhaven National Laboratory under Contract No. DE-SC0012704. Work at the Molecular Foundry was supported by the Office of Science, Office of Basic Energy Sciences, of the U.S. Department of Energy under Contract No. DE-AC02-05CH11231. The authors acknowledge the NREL HPC resources for providing computing facilities under the ahlssic allocation. This research was supported by Umicore, Contract Number 34586 to the Regents of the University of California, Berkeley. G.W. acknowledges support by the U.S. Department of Energy, Office of Science, Office of Advanced Scientific Computing Research, Department of Energy Computational Science Graduate Fellowship under Award Number DE-SC0023112. This report was prepared as an account of work sponsored by an agency of the United States Government. Neither the United States Government nor any agency thereof, nor any of their employees, makes any warranty, express or implied, or assumes any legal liability or responsibility for the accuracy, completeness, or usefulness of any information, apparatus, product, or process disclosed, or represents that its use would not infringe privately owned rights. Reference herein to any specific commercial product, process, or service by trade name, trademark, manufacturer, or otherwise does not necessarily constitute or imply its endorsement, recommendation, or favoring by the United States Government or any agency thereof. The views and opinions of authors expressed herein do not necessarily state or reflect those of the United States Government or any agency thereof. H.J. acknowledges support by NSF Grant 2145832.

■ REFERENCES

(1) Famprikis, T.; Canepa, P.; Dawson, J. A.; Islam, M. S.; Masquelier, C. Fundamentals of Inorganic Solid-State Electrolytes for Batteries. *Nat. Mater.* **2019**, *18* (12), 1278−1291.

(2) Yang, X.; Adair, K. R.; Gao, X.; Sun, X. Recent Advances and Perspectives on Thin Electrolytes for High-Energy-Density Solid-State Lithium Batteries. *Energy Environ. Sci.* **2021**, *14* (2), 643−671.

(3) Zhao, Q.; Stalin, S.; Zhao, C.-Z.; Archer, L. A. Designing Solid-State Electrolytes for Safe, Energy-Dense Batteries. *Nat. Rev. Mater.* **2020**, *5* (3), 229−252.

(4) Jun, K.; Chen, Y.; Wei, G.; Yang, X.; Ceder, G. Diffusion Mechanisms of Fast Lithium-Ion Conductors. *Nat. Rev. Mater.* **2024**, *9*, 887−905.

(5) Liu, Y.-K.; Zhao, C.-Z.; Du, J.; Zhang, X.-Q.; Chen, A.-B.; Zhang, Q. Research Progresses of Liquid Electrolytes in Lithium-Ion Batteries. *Small* **2023**, *19* (8), No. 2205315.

(6) Chen, X.; Guan, Z.; Chu, F.; Xue, Z.; Wu, F.; Yu, Y. Air-Stable Inorganic Solid-State Electrolytes for High Energy Density Lithium Batteries: Challenges, Strategies, and Prospects. *InfoMat* **2022**, *4* (1), No. e12248.

(7) Huang, L.; Zhang, L.; Bi, J.; Liu, T.; Zhang, Y.; Liu, C.; Cui, J.; Su, Y.; Wu, B.; Wu, F. An Insight into Halide Solid-State Electrolytes: Progress and Modification Strategies. *Energy Material Advances* **2024**, *4*, No. 0092.

(8) Zhao, X.; Zhao-Karger, Z.; Fichtner, M.; Shen, X. Halide-Based Materials and Chemistry for Rechargeable Batteries. *Angew. Chem., Int. Ed.* **2020**, *59* (15), 5902−5949.

(9) Yang, X.; Gupta, S.; Chen, Y.; Sari, D.; Hau, H.-M.; Cai, Z.; Dun, C.; Qi, M.; Ma, L.; Liu, Y.; Urban, J. J.; Ceder, G. Fast Room-Temperature Mg-Ion Conduction in Clay-Like Halide Glassy Electrolytes. *Adv. Energy Mater.* **2024**, *14* (26), No. 2400163.

(10) Li, X.; Liang, J.; Yang, X.; Adair, K. R.; Wang, C.; Zhao, F.; Sun, X. Progress and Perspectives on Halide Lithium Conductors for All-Solid-State Lithium Batteries. *Energy Environ. Sci.* **2020**, *13* (5), 1429−1461.

(11) Asano, T.; Sakai, A.; Ouchi, S.; Sakaida, M.; Miyazaki, A.; Hasegawa, S. Solid Halide Electrolytes with High Lithium-Ion Conductivity for Application in 4 V Class Bulk-Type All-Solid-State Batteries. *Adv. Mater.* **2018**, *30* (44), No. 1803075.

(12) Nie, X.; Hu, J.; Li, C. Halide-Based Solid Electrolytes: The History, Progress, and Challenges. *Interdisciplinary Materials* **2023**, *2* (3), 365−389.

(13) Nikodimos, Y.; Su, W.-N.; Hwang, B. J. Halide Solid-State Electrolytes: Stability and Application for High Voltage All-Solid-State Li Batteries. *Adv. Energy Mater.* **2023**, *13* (3), No. 2202854.

(14) Zheng, M.; Li, X.; Sun, J.; Wang, X.; Liu, G.; Yu, W.; Dong, X.; Wang, J. Research Progress on Chloride Solid Electrolytes for All-Solid-State Batteries. *J. Power Sources* **2024**, *595*, No. 234051.

(15) Wu, H.; Han, H.; Yan, Z.; Zhao, Q.; Chen, J. Chloride Solid-State Electrolytes for All-Solid-State Lithium Batteries. *J. Solid State Electrochem* **2022**, *26* (9), 1791−1808.

(16) Li, X.; Liang, J.; Luo, J.; Norouzi Banis, M.; Wang, C.; Li, W.; Deng, S.; Yu, C.; Zhao, F.; Hu, Y.; Sham, T.-K.; Zhang, L.; Zhao, S.; Lu, S.; Huang, H.; Li, R.; Adair, K. R.; Sun, X. Air-Stable Li 3 InCl 6 Electrolyte with High Voltage Compatibility for All-Solid-State Batteries. *Energy Environ. Sci.* **2019**, *12* (9), 2665−2671.

(17) Zhou, L.; Kwok, C. Y.; Shyamsunder, A.; Zhang, Q.; Wu, X.; Nazar, L. F. A New Halospinel Superionic Conductor for High-Voltage All Solid State Lithium Batteries. *Energy Environ. Sci.* **2020**, *13* (7), 2056−2063.

(18) Liang, J.; Li, X.; Wang, S.; Adair, K. R.; Li, W.; Zhao, Y.; Wang, C.; Hu, Y.; Zhang, L.; Zhao, S.; Lu, S.; Huang, H.; Li, R.; Mo, Y.; Sun, X. Site-Occupation-Tuned Superionic LixScCl3+xHalide Solid Electrolytes for All-Solid-State Batteries. *J. Am. Chem. Soc.* **2020**, *142* (15), 7012−7022.
(19) Riegger, L. M.; Schlem, R.; Sann, J.; Zeier, W. G.; Janek, J. Lithium-Metal Anode Instability of the Superionic Halide Solid Electrolytes and the Implications for Solid-State Batteries. *Angew. Chem., Int. Ed.* **2021**, *60* (12), 6718−6723.
(20) Cros, C.; Hanebali, L.; Latie, L.; Villeneuve, G.; Gang, W. Structure, Ionic Motion and Conductivity in Some Solid-Solutions of the LiClMCl2 Systems (M═Mg,V,Mn). *Solid State Ionics* **1983**, *9*−*10*, 139−147.
(21) Kanno, R.; Takeda, Y.; Takada, K.; Yamamoto, O. Ionic Conductivity and Phase Transition of the Spinel System Li2 − 2x M 1 + x Cl4 (M = Mg, Mn, Cd). *J. Electrochem. Soc.* **1984**, *131* (3), 469.
(22) Steiner, H. J.; Lutz, H. D. Structural Phase Transitions of Fast Lithium Ion Conductors Li2MIICl4 (MII = Mg, Mn, Cd). *J. Solid State Chem.* **1992**, *99* (1), 1−11.
(23) Gao, Z.; Wang, S.; Sun, F.; Yu, Z.; Song, H.; Liu, Z.; Chen, H. Enhanced Electrochemical Properties of Li2MgCl4 by Zn Substitution for All-Solid-State Batteries. *J. Solid State Chem.* **2023**, *328*, No. 124361.
(24) Tan, H.-Y.; Zhou, M.-Y.; Huang, Z.; Luo, J.-D.; Yang, J.-T.; Wang, J.-P.; Wu, Y.-C.; Cheng, X.-B.; Wang, Z.-W.; Hao, X.-D.; Wang, L.; Gong, K.; Yin, Y.-C.; Xiao, Y.; Yao, H.-B. Low Cost and Low Density Chloride Solid Electrolyte for All Solid State Cathode with High Active Material Ratio. *Nano Res.* **2024**, *17*, 8826.
(25) Rom, C. L.; Yox, P.; Cardoza, A. M.; Smaha, R. W.; Phan, M. Q.; Martin, T. R.; Maughan, A. E. Expanding the Phase Space for Halide-Based Solid Electrolytes: Li−Mg−Zr−Cl Spinels. *Chem. Mater.* **2024**, *36* (15), 7283−7291.
(26) Deng, B.; Zhong, P.; Jun, K.; Riebesell, J.; Han, K.; Bartel, C. J.; Ceder, G. CHGNet as a Pretrained Universal Neural Network Potential for Charge-Informed Atomistic Modelling. *Nat. Mach Intell* **2023**, *5* (9), 1031−1041.
(27) Vandermause, J.; Xie, Y.; Lim, J. S.; Owen, C. J.; Kozinsky, B. Active Learning of Reactive Bayesian Force Fields Applied to Heterogeneous Catalysis Dynamics of H/Pt. *Nat. Commun.* **2022**, *13* (1), 5183.
(28) Soubeyroux, J. L.; Cros, C.; Gang, W.; Kanno, R.; Pouchard, M. Neutron Diffraction Investigation of the Cationic Distribution in the Structure of the Spinel-Type Solid Solutions Li2−2xM1+xCl4 (M = Mg, V): Correlation with the Ionic Conductivity and NMR Data. *Solid State Ionics* **1985**, *15* (4), 293−300.
(29) Chen, Y.; Lun, Z.; Zhao, X.; Koirala, K. P.; Li, L.; Sun, Y.; O'Keefe, C. A.; Yang, X.; Cai, Z.; Wang, C.; Ji, H.; Grey, C. P.; Ouyang, B.; Ceder, G. Unlocking Li Superionic Conductivity in Face-Centred Cubic Oxides via Face-Sharing Configurations. *Nat. Mater.* **2024**, *23* (4), 535−542.
(30) Zhang, W.; Seo, D.-H.; Chen, T.; Wu, L.; Topsakal, M.; Zhu, Y.; Lu, D.; Ceder, G.; Wang, F. Kinetic Pathways of Ionic Transport in Fast-Charging Lithium Titanate. *Science* **2020**, *367* (6481), 1030−1034.
(31) Yang, J. H.; Ceder, G. Activated Internetwork Pathways in Partially-Disordered Spinel Cathode Materials with Ultrahigh Rate Performance. *Adv. Energy Mater.* **2023**, *13* (4), No. 2202955.
(32) Ji, H.; Wu, J.; Cai, Z.; Liu, J.; Kwon, D.-H.; Kim, H.; Urban, A.; Papp, J. K.; Foley, E.; Tian, Y.; Balasubramanian, M.; Kim, H.; Clément, R. J.; McCloskey, B. D.; Yang, W.; Ceder, G. Ultrahigh Power and Energy Density in Partially Ordered Lithium-Ion Cathode Materials. *Nat. Energy* **2020**, *5* (3), 213−221.
(33) Chen, T.; Yang, J.; Barroso-Luque, L.; Ceder, G. Removing the Two-Phase Transition in Spinel LiMn2O4 through Cation Disorder. *ACS Energy Lett.* **2023**, *8* (1), 314−319.

https://doi.org/10.1021/acsenergylett.5c00078
ACS Energy Lett. 2025, 10, 1338−1346